Chinese Journal of Chemical Engineering 95 (2026) 226–239

Contents lists available at ScienceDirect

Chinese Journal of Chemical Engineering

journal homepage: www.elsevier.com/locate/CJChE

Full Length Article

Gas–liquid countercurrent absorption process based on micro-scale helical liquid-bridge flow

Liang Yuan [1, #], Xiaoxuan Chen [1, #], Haifeng Cong [1, 2, *], Xingang Li [1, 2, *]

[1] School of Chemical Engineering and Technology, National Engineering Research Center of Distillation Technology, Collaborative Innovation Center of Chemical Science and Engineering (Tianjin), Tianjin University, Tianjin 300072, China
[2] Zhejiang Institute of Tianjin University, Ningbo 315201, China

ARTICLE INFO

Article history:
Received 8 January 2026
Received in revised form
19 March 2026
Accepted 22 March 2026
Available online 13 April 2026

Keywords:
Helical liquid-bridge flow
Micro-scale gas–liquid countercurrent flow
Dimensionless correlation
Gas–liquid absorption

ABSTRACT

Achieving efficient gas–liquid countercurrent operation in microreactors faces multiple technical challenges, primarily due to the difficulty in forming stable countercurrent flow naturally, along with high flow resistance and substantial pressure drop. This study proposes a novel microscale gas–liquid countercurrent absorption method based on helical liquid-bridge flow. Micron-scale helical structures are employed to induce stable semi-constrained liquid-bridges, enabling controlled countercurrent contact. By adjusting helical parameters and feed configurations, the method optimizes liquid film distribution, residence time, and interfacial renewal, thereby enhancing mass transfer. Experiments in a CO_2–water system showed that the volumetric mass transfer coefficient increased by 1–2 orders of magnitude compared to conventional devices. A dimensionless correlation for the liquid-phase mass transfer coefficient was developed with less than 15% deviation. This work provides a theoretical and technical foundation for developing efficient microscale gas–liquid absorption devices, with broad applicability in process intensification and system integration of microchemical engineering.
© 2026 The Chemical Industry and Engineering Society of China, and Chemical Industry Press Co., Ltd. All rights are reserved, including those for text and data mining, AI training, and similar technologies.

1. Introduction

Gas–liquid countercurrent operation, as a core technology in multistage precision distillation and absorption processes, holds significant importance in chemical production due to its ability to substantially enhance heat and mass transfer efficiency as well as reaction kinetics performance [1–3]. Traditional countercurrent tower equipment, leveraging mature processes and strong processing capacity, is widely used in industrial separation processes [4–8]. However, its mass transfer efficiency is constrained by equipment size and fluid dynamic characteristics. Research indicates that the volumetric mass transfer coefficients of conventional tower equipment typically range only from 0.01 to 0.1 s^{-1}, and the equipment is notably bulky [9,10]. As process intensification technologies advance, the limitations of traditional equipment become increasingly apparent; they fail to meet modern industry's demand for efficient and compact separation units [11]. Furthermore, large absorption towers suffer from high energy consumption and poor operational flexibility, issues that are particularly pronounced in the context of green chemical engineering and energy conservation efforts.

The emergence of microchemical engineering technology provides a new technical pathway for the transformation of chemical manufacturing toward precision, flexibility, and environmental sustainability [12–15]. This technology reduces fluid channel dimensions from the millimeter scale to the micrometer scale. Such miniaturization increases the specific surface area of microreactors by two to three orders of magnitude compared to conventional tower equipment, significantly expanding the gas–liquid contact area and enhancing mass transfer efficiency [16–19]. However, countercurrent gas–liquid operation within microreactors still faces technical challenges. In conventional tower equipment, countercurrent gas–liquid flow relies primarily on the density difference between the two phases. At the micro scale, surface forces replace gravity as the dominant force, rendering the traditional countercurrent mechanism ineffective and making it difficult to establish stable natural countercurrent flow [20]. Additionally, reduced microchannel dimensions increase two-phase flow resistance, leading to significant localized pressure drops. Although methods such as multi-inlet and multi-outlet configurations or optimized channel geometries can

* Corresponding authors.
E-mail addresses: conghaifeng@tju.edu.cn (H. Cong), lxg@tju.edu.cn (X. Li).
These authors contributed equally to this work.

https://doi.org/10.1016/j.cjche.2026.03.013
1004-9541/© 2026 The Chemical Industry and Engineering Society of China, and Chemical Industry Press Co., Ltd. All rights are reserved, including those for text and data mining, AI training, and similar technologies.

alleviate these issues [21], they also increase fabrication complexity and manufacturing costs [14,22]. Moreover, achieving large-area stable countercurrent flow at the microscale remains challenging, thereby limiting industrial applicability. Consequently, exploring innovative microscale flow patterns that balance structural simplicity, cost control, and stable, efficient countercurrent contact has become a critical breakthrough issue in this field.

The concept of helical liquid-bridge flow (Fig. 1) offers a solution to the aforementioned challenge. Cong *et al.* [23] found that liquid forms overlapping structures within the helical gaps, rapidly establishing a continuous and stable helical liquid-bridge flow pattern that spirals downward along the helical line. This flow pattern belongs to semi-constrained flow, which is distinct from unconstrained flow and fully constrained flow. In unconstrained flow, one phase (gas or liquid) acts as the dispersed phase, typically existing in parallel or fully mixed flow configurations, making it more suitable for reaction processes; fully constrained flow relies entirely on pipeline structures to define gas–liquid flow paths, making countercurrent operation difficult to achieve. Semi-constrained flow utilizes structured packing, trays, catalysts, and similar carriers to constrain and control liquid phase flow through interfacial interactions. This ensures both gas and liquid phases remain continuous within the apparatus, facilitating the formation of stable countercurrent contact. Compared to the liquid film flow in traditional falling film reactors, spiral liquid-bridge flow exhibits fundamental differences and significant advantages. In conventional falling film reactors, the liquid spreads along the wall surface solely by gravity to form a single liquid film, with gas–liquid contact confined to the outer surface of the liquid film. In contrast, spiral liquid-bridge flow utilizes the guiding effect of a helical line to form a liquid-bridge structure with both inner and outer free surfaces, enabling gas–liquid contact to occur simultaneously on both the inner and outer surfaces of the liquid film. Unlike the aforementioned microchannel structures which require complex microfabrication processes, the helical liquid-bridge achieves spontaneous, stable countercurrent gas–liquid mixing through a simple helical configuration. This eliminates cumbersome microfabrication, significantly reducing costs and operational complexity. This clearly defined flow path not only provides greater interfacial area but also reduces gas-phase flow resistance, thereby enhancing interfacial stability and mass transfer driving forces. Moreover, the feasibility of micro-scale helical liquid-bridge flow has been demonstrated in prior research [24,25] and has established a foundation in liquid-phase hydrodynamics for efficient gas–liquid countercurrent operation in microreactors. Therefore, helical liquid-bridge flow offers a promising approach to achieving stable gas–liquid countercurrent flow at the microscale, with the potential to overcome current limitations in mass transfer technologies.

This study focuses on investigating the flow characteristics and mass transfer performance of microscale helical liquid-bridges. It systematically analyzes the flow paths of the gas and liquid phases and experimentally determined key parameters, including the average residence time, liquid film thickness, and effective mass transfer area, to elucidate the mass transfer mechanism. Based on these data, the influence of gas-phase velocities inside, outside, and on both sides of the channel on mass transfer was examined. The regulatory effects of liquid-phase velocity and spring structural parameters, such as pitch and diameter, on the mass transfer process were also analyzed. A predictive model for the mass transfer coefficient was developed using experimental data, providing a theoretical basis and technical support for the development of a new generation of highly efficient microscale gas–liquid countercurrent absorption equipment.

2. Materials and Methods

2.1. Fluid flow experiment

To date, systematic reports on the flow behavior and gas–liquid interactions in microscale gas–liquid two-phase liquid-bridge flows have remained scarce. To investigate the characteristics of such two-phase flow, the experimental setup shown in Fig. 2 was used. The apparatus included dual gas inlets (Inlet 1 and Inlet 2), dual gas outlets, and a single liquid inlet and outlet. The helical wire was vertically mounted, connected at the top to a liquid distributor with gas channels and at the bottom to a restrictor also equipped with gas channels. The liquid phase was injected into the apparatus using a syringe pump (2 PB-2020, SZWEICO, China), overflowed through the distributor onto the helical wire, and finally exited through the outlet. The gas phase was split into two streams: one entered the external channel of the helical wire from the side wall of the apparatus through Inlet 1, and the other entered the internal channel through Inlet 2 *via* the restrictor. The gas flow path could be selected individually for the external channel, internal channel, or two channels simultaneously. Polystyrene microspheres with a particle size of 100 μm were used to track liquid-phase flow. The physical properties of

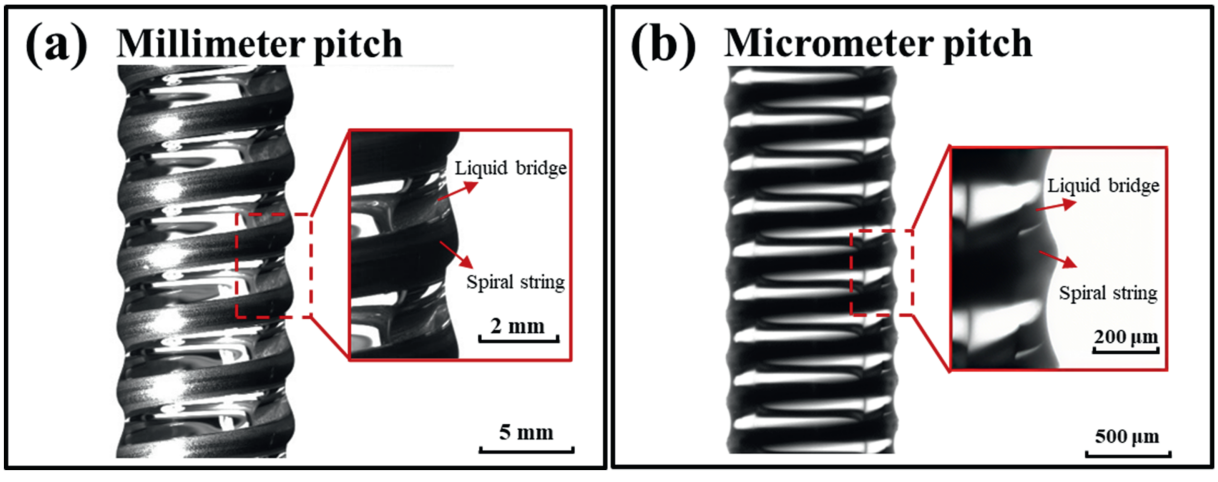


Fig. 1. Schematic diagrams of helical liquid-bridge flow: (a) millimeter-scale liquid-bridge flow, (b) micrometer-scale liquid-bridge flow.

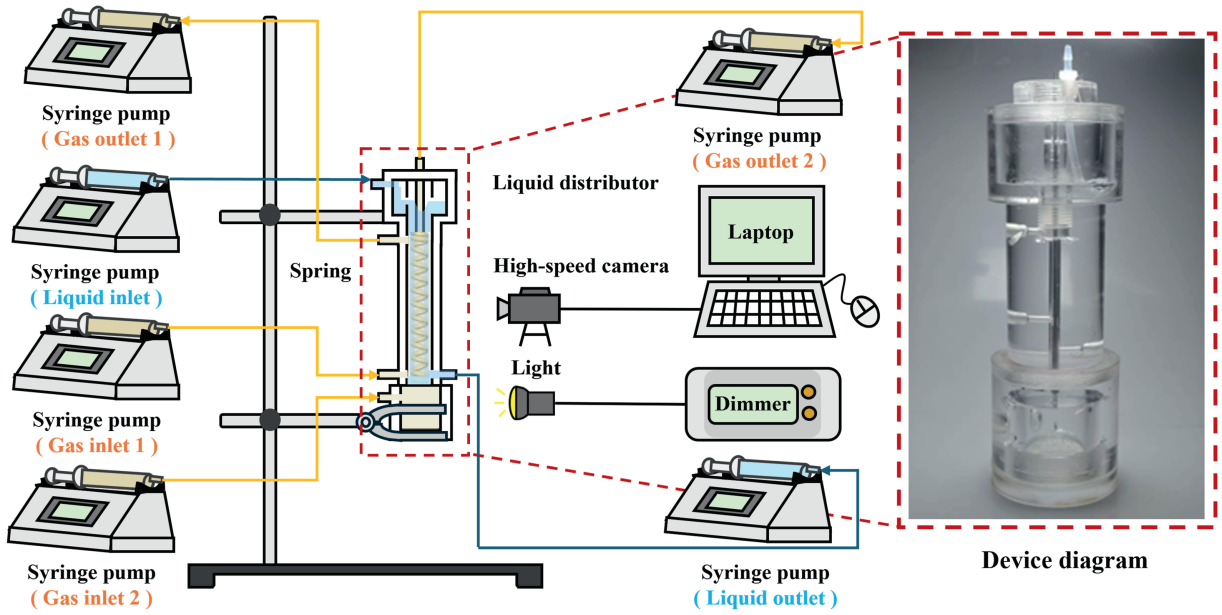


Fig. 2. Gas–liquid two-phase fluid flow experimental setup.

the microspheres are listed in Table 1. The density of the polystyrene microspheres is very close to that of water, effectively suppressing sedimentation effects and ensuring they can effectively follow the water-phase flow. Nitrogen dioxide gas, generated by the reaction between concentrated nitric acid and copper foil, served as a colorimetric tracer for the gas phase. Syringe pumps precisely controlled the flow rates of both phases to ensure a continuous and stable experimental process. High-speed cameras (1M – 2000, AcutEye, China) recorded the flow behavior of both phases for subsequent analysis of gas–liquid interactions and flow characteristics.

Its internal core component features a helical structure with micrometer-level pitch, as shown in Fig. 3. The geometric parameters of the helix primarily included five key dimensions: length H, diameter D, pitch W, wire diameter d, and helix angle θ. The helix length was determined by the requirements of the gas–liquid contact channel, while the diameter selection balanced the gas-phase contact area inside and outside the helix. The pitch influenced the gas–liquid contact area, and the wire diameter determined the mechanical strength of the helix. The selection criteria for the geometric parameters of the helical structure and the operating conditions in the experiment were based on the formation of a continuous and stable liquid-bridge along the helical line. The critical capillary length of a liquid-bridge can be calculated using the Young–Laplace equation [26,27]:

$$l_c = \sqrt{\frac{\gamma}{\rho g}} \tag{1}$$

Table 1
Physical properties of the tracer particles.

Parameter	Value
Microsphere composition	Polystyrene
Mean particle size/μm	100
Microsphere density/g·cm^{-3}	1.05
Refractive index (@589 nm)	1.59
Dispersion composition	Polystyrene microsphere aqueous dispersion

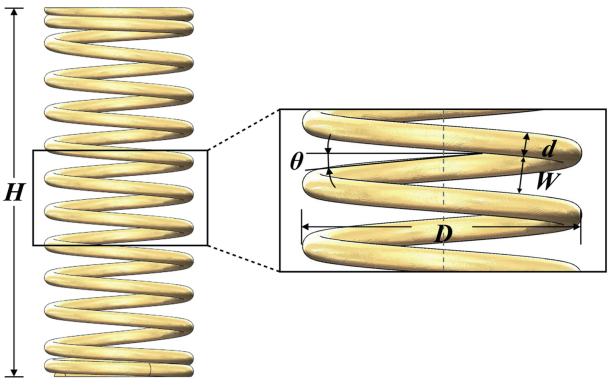


Fig. 3. Schematic diagram of a micron-scale helical structure.

where γ is the surface tension at the gas–liquid interface, ρ is the liquid phase density, g is the gravitational acceleration. The specific parameters of the helices used in the experiment are listed in Table 2. All helices were manufactured by Kaily Spring Company (China) and made of stainless steel, with the wire surface mechanically polished to be clean and smooth, and contact angle measurement procedures were shown in the Supplementary Material.

To quantitatively characterize fluid flow and mass transfer processes within micro-scale helical liquid-bridges, thereby enabling accurate process description, rational design, and optimization, this study experimentally determined key

Table 2
Table of geometric parameters of helixes.

Project	Value
Helical string height, H/mm	50
Helical string diameter, D/mm	2, 2.1
Helical string pitch, W/μm	150, 300, 450
Helical string diameter, d/mm	0.25, 0.3

hydrodynamic parameters including average residence time, average liquid film thickness, and effective mass transfer area. The specific measurement methods are as follows:

Average liquid film thickness. Once the liquid-bridge flow had stabilized, images of the liquid-bridge were captured using a high-speed camera. The images were processed with ImageJ180 to obtain the liquid film neckline distance, from which the liquid film thickness was derived. Because both the inner and outer surfaces of the liquid-bridge contribute to mass transfer, the effective mass transfer liquid film thickness was taken as half of the total liquid film thickness.

Gas–liquid contact area. As the liquid phase flows spirally through the helical gaps, each gap is filled and wetted. Thus, no mass transfer dead zones are present on the micro-scale helical structure. The effective gas–liquid contact area equals the sum of the inner and outer surface areas of the liquid-bridge unfolding along the helical path. The calculation method for the gas–liquid contact area is as follows. Define L_C as the arc length of the liquid-bridge boundary, calculated using the arc length formula:

$$L_C = 2\alpha R \tag{2}$$

Define L_F as the actual path of the liquid-bridge flowing along the helix gap, which can be calculated using the following equation:

$$L_F = \sqrt{H^2 + (N\pi D)^2} \tag{3}$$

Since both the inner and outer surfaces of the liquid-bridge serve as gas–liquid contact areas, its total gas–liquid contact area is the sum of the effective mass transfer areas on the inner and outer sides of the liquid-bridge. This can be calculated using the following equation:

$$S = L_C L_{F,in} + L_C L_{F,out} \tag{4}$$

Average residence time. Polystyrene microspheres with a diameter of 100 μm were used as tracer particles in the liquid phase. After the liquid-bridge flow reached a stable state, the tracer particles were injected from the top and allowed to move downward along the helical path with the liquid. A high-speed camera recorded the time at which the particles entered and exited the helical structure, and the residence time was calculated accordingly. The experiment was repeated three times under identical operating conditions, and the arithmetic mean of the three results was taken as the average residence time.

2.2. Mass transfer experiment

Countercurrent mass transfer experiments were conducted using a carbon dioxide absorption model system. The experimental apparatus is shown in Fig. 4. Carbon dioxide with a purity of 99.9% (molar fraction) was used as the gas source, and its flow rate was regulated by a mass flow controller (ACU20FD-LC, Beijing Jingliang Technology Co., Ltd., China). The gas entered the apparatus from the bottom (inside the spiral) and the side wall (outside the spiral), then flowed upward in countercurrent mode along the inner and outer channels of the spiral. The gas was finally collected using a gas collection bag. Deionized water was employed as the absorbent and injected into the distributor *via* a syringe pump. It flowed downward along the spiral under gravity and exited through the outlet. During the experiments, the gas and liquid phases formed a stable spontaneous countercurrent flow, and their flow paths remained distinct without mutual interference. Absorbent liquid samples were collected at the outlet. Each sample was mixed with 0.05 $mol \cdot L^{-1}$ barium hydroxide solution and titrated with 0.1 $mol \cdot L^{-1}$ hydrochloric acid to determine the carbon dioxide concentration. All experimental sets were repeated three times, and the results were averaged to ensure data reliability.

Various mass transfer models have been proposed to describe the absorption of gases in liquids, such as the film model, surface renewal model, and permeation model. Based on the research by Lokhat *et al.* [28], Zhang *et al.* [29], and Chen *et al.* [30], and the conditions of this experiment, the film model is more appropriate. At ambient temperatures, carbon dioxide exhibits low solubility in water, with mass transfer resistance primarily concentrated in the liquid film. Consequently, the overall liquid-phase mass transfer coefficient approximates the total mass transfer coefficient. Based on the dual-film theory, the mass transfer rate equation expressed in terms of liquid-phase concentration as the driving force is:

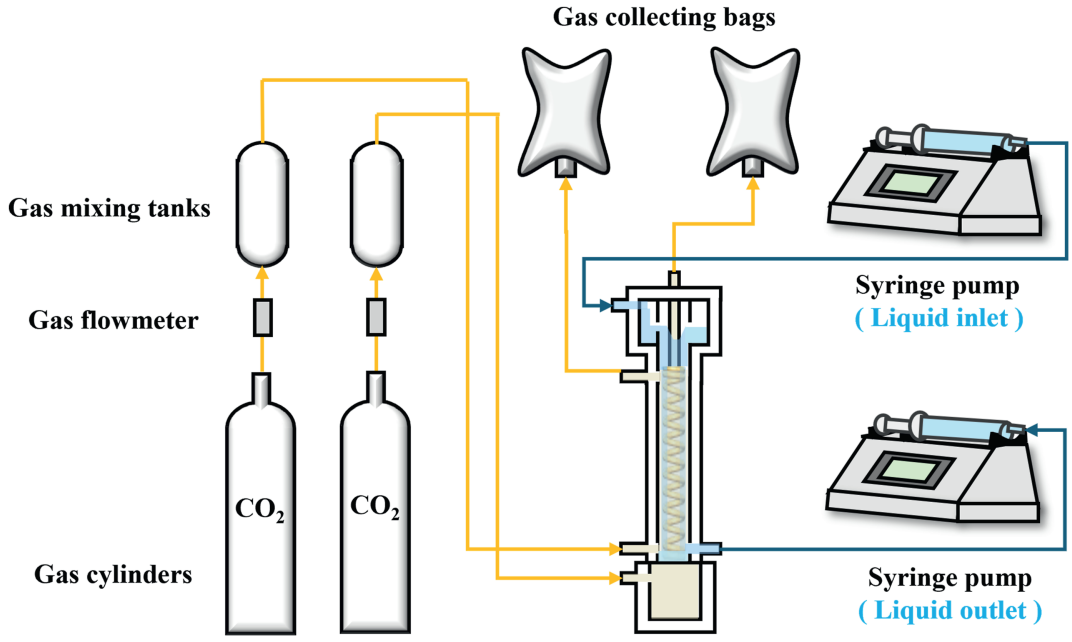


Fig. 4. Experimental setup for gas–liquid countercurrent mass transfer.

$$G = K_L A\left(C^*_{CO_2} - C_{CO_2}\right) \tag{5}$$

where G represents the mass transfer rate, K_L denotes the overall mass transfer coefficient driven by the liquid-phase concentration, A signifies the interfacial area between the two phases, $C^*_{CO_2}$ indicates the gas-phase equilibrium concentration, and C_{CO_2} represents the average concentration of the CO_2 component in the liquid phase. $C^*_{CO_2}$ is calculated using Dalton's law of partial pressures and Henry's law:

$$C^*_{CO_2} = Hp_{CO_2} \tag{6}$$

where p_{CO_2} represents the total system pressure, and H denotes the solubility coefficient. Within a unit length differential segment of the spiral, the material balance equation is:

$$\frac{dG}{dh} = K_L aS\left(C^*_{CO_2} - C_{CO_2}\right) \tag{7}$$

where a is the specific surface area of gas–liquid contact, and S is the cross-sectional area of the micro-spiral structure. Define the liquid-phase volumetric flow rate as V. Integrating the formula along the height of the spiral yields:

$$h = \frac{V}{K_L aS} \cdot \int_{C_{CO_2,in}}^{C_{CO_2,out}} \frac{dC_{CO_2}}{C^*_{CO_2} - C_{CO_2}} \tag{8}$$

Calculate the height of the mass transfer unit using the average driving force method:

$$h = \frac{V}{K_L aS} \cdot \frac{C_{CO_2,out} - C_{CO_2,in}}{\Delta C_{CO_2,m}} \tag{9}$$

where $\Delta C_{CO_2,m}$ is the average driving force in the liquid phase:

$$\Delta C_{CO_2,m} = \frac{\left(C^*_{CO_2,in} - C_{CO_2,in}\right) - \left(C^*_{CO_2,out} - C_{CO_2,out}\right)}{\ln \frac{C^*_{CO_2,in} - C_{CO_2,in}}{C^*_{CO_2,out} - C_{CO_2,out}}} \tag{10}$$

The entire mass transfer process is governed by resistance concentrated in the liquid film, making it a liquid film-controlled process. Consequently, the volumetric mass transfer coefficient on the liquid side equals the overall volumetric mass transfer coefficient of the liquid phase:

$$k_l a = K_L a = \frac{V}{hS} \cdot \frac{C_{CO_2,out} - C_{CO_2,in}}{\Delta C_{CO_2,m}} \tag{11}$$

3. Results and Discussion

3.1. Two-phase flow pattern

Under conditions where N_2 was injected into both the inner and outer sides of the gas channel, a small amount of polystyrene microspheres was added to the liquid phase as tracer particles. The particles flowed with the liquid-bridge and filled the helical spring gaps. A high-definition camera recorded this process, and the particle trajectories are shown in Video 1 (in Supplementary Material). Slow-motion playback (Fig. 5) showed that the tracer particles within the helical spring gap flowed downward along the spiral direction and covered equal descent heights within identical time intervals. The liquid-bridge morphology remained stable, indicating that a stable microscale helical liquid-bridge flow had formed along the helical structure.

Supplementary video related to this article can be found at https://doi.org/10.1016/j.cjche.2026.03.013

After the feasibility of microscale liquid-bridge flow was confirmed, further investigation into the gas flow behavior within the two-phase system was conducted. Under stable liquid-bridge flow conditions, nitrogen dioxide (NO_2) was used as a tracer gas to visualize the gas flow path. Three gas injection configurations were tested: injection through the inner channel only (Fig. 6(a)), injection through the outer channel only (Fig. 6(b)), and simultaneous injection through both inner and outer channels (Fig. 6(c)). The gas entered the apparatus through the respective inlets, flowed into the corresponding spiral channels according to the inlet position, contacted the liquid phase countercurrently, and was finally discharged from the top outlet. The distribution of the tracer gas consistently corresponded to the injection location: it was confined to the inner region during inner-channel injection (Fig. 6(d)), to the outer region during outer-channel injection (Fig. 6(e)), and was present in both regions during simultaneous injection (Fig. 6(f)). These results indicate that the system allows flexible and controllable countercurrent gas–liquid contact, resulting in three distinct operational modes.

It is noteworthy that under the experimental conditions employed, the countercurrent flow of gas does not interfere with the liquid descent process. However, when the gas flow intensity increases significantly, the coupling effect between the gas and liquid phases may become pronounced, necessitating further verification of the flow patterns in both phases.

3.2. Fluid flow behavior

3.2.1. Liquid-bridge morphology

Fig. 7(a) shows a schematic diagram of the geometric reconstruction of the liquid-bridge cross-section. The key structural parameters of the liquid-bridge include the mid-width (M) and the arc lengths (L_C) on both sides. These geometric parameters collectively determine the contour and interfacial characteristics of the liquid-bridge. Fig. 7(b)–(g) present experimental results illustrating variations in the liquid-bridge contour morphology with liquid phase load for helical structures with different parameters. As the liquid phase load increased, the liquid-bridge contour expanded outward, resulting in an increase in the M. An increase in pitch reduced the M of the liquid-bridge, leading to a narrower and more elongated shape. The greater axial distance between adjacent helical wires induced longitudinal stretching of the liquid-bridge under the combined effects of gravity and surface tension. To conserve liquid volume and minimize interfacial energy, the liquid-bridge extended axially while contracting laterally. In contrast, an increase in wire diameter resulted in a larger M. The enhanced solid–liquid contact area facilitated lateral spreading of the liquid over the solid surface. Additionally, an increase in helix diameter slightly reduced the M of the liquid-bridge. The same volume of liquid was distributed over a longer flow path, and under the constraints of interfacial tension and volume conservation, the liquid-bridge contracted inward to maintain morphological stability.

Thus, both liquid phase loading and helical structure parameters (pitch, wire diameter, and helix diameter) significantly influenced liquid-bridge morphology. Consequently, optimizing liquid-bridge shape can be achieved through rational design of helical structure parameters.

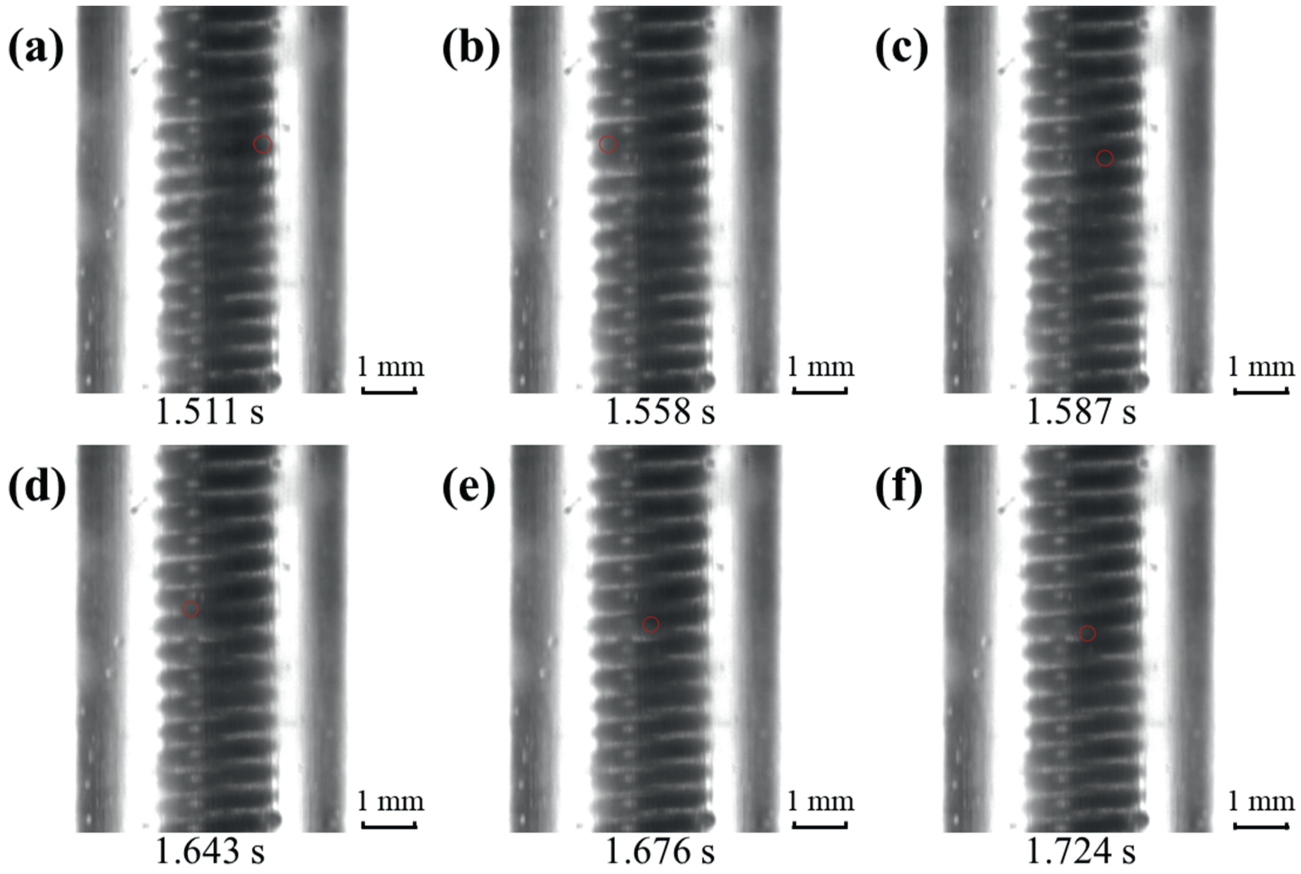


Fig. 5. Snapshot of tracer particle trajectory.

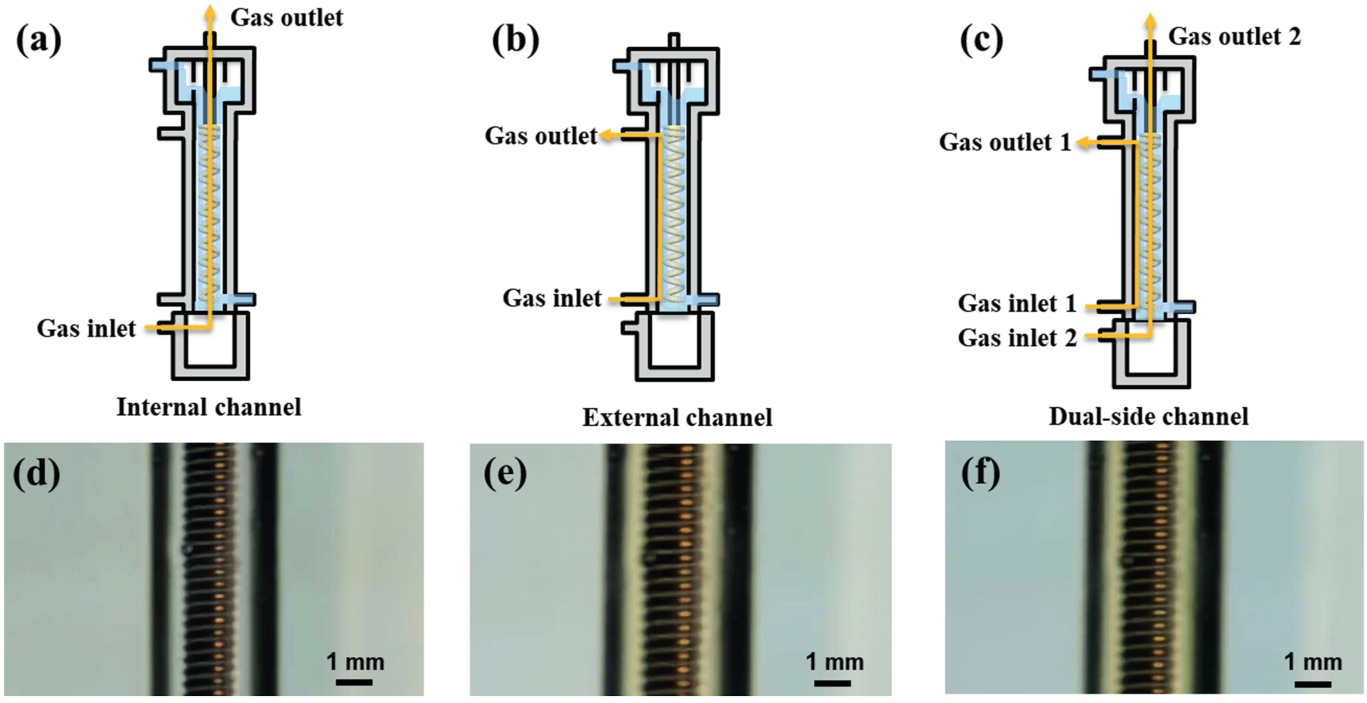


Fig. 6. Schematics of two-phase flow gas paths: (a) and (d) injection into inner channel, (b) and (e) injection into outer channel, (c) and (f) injection into two channels.

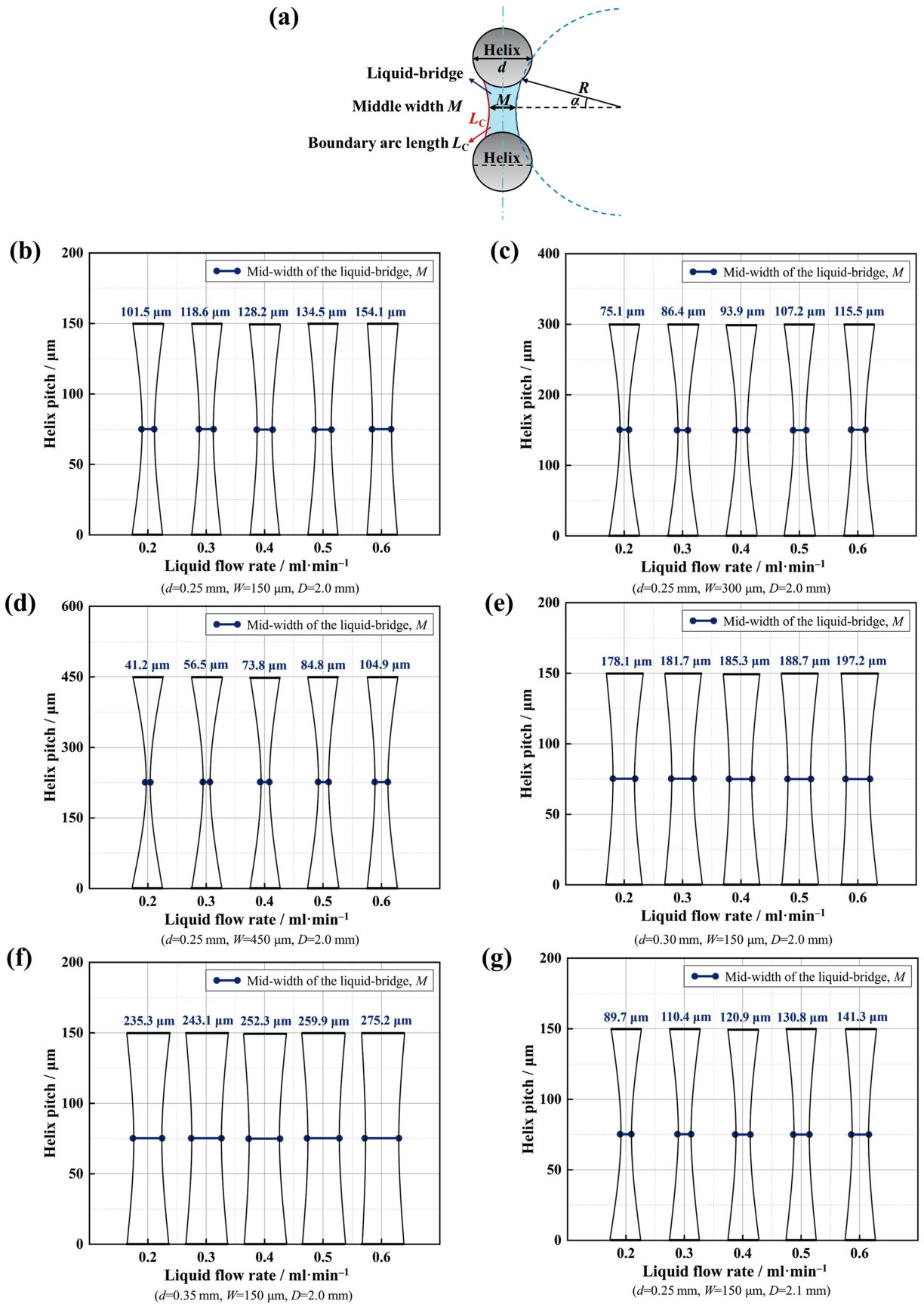


Fig. 7. Changes in liquid-bridge profile: (a) schematic cross-section of liquid-bridge, (b)–(g) trends in liquid-bridge profile changes.

3.2.2. Average liquid film thickness

The thickness of the liquid film crucially influences mass transfer performance. Given the variability of the liquid-bridge flow interface and the complexity of parameter calculation, the cross-section was simplified under the following assumptions: (1) The effect of gravity on the cross-sectional morphology of the liquid-bridge was neglected. (2) The circles corresponding to the left and right arcs pass through the midpoint of the liquid-bridge boundary and the point of intersection between the generatrix of the spring's circumscribed cylinder and the spring wire. Based on these assumptions, the three-point method was used to determine the arc length, which allowed the wetted perimeter and the upper and lower arc lengths to be established, ultimately yielding the cross-sectional area, S_C, of the liquid-bridge (see the Supplementary Material for details). Owing to the hollow structure of the liquid-bridge, both its inner and outer surfaces act as gas–liquid contact areas. Therefore, the average liquid film thickness, δ, was taken as half of the full liquid-bridge thickness. The average liquid film thickness was calculated by dividing the cross-sectional area of the liquid-bridge by twice the pitch:

$$\delta = \frac{S_C}{2W} \tag{12}$$

Fig. 8 shows the variation of average liquid film thickness with liquid phase loading. As indicated in the figure, the average liquid film thickness of the liquid-bridge gradually increased with increasing liquid phase loading. In contrast, the average liquid film thickness decreased slightly with increasing helix diameter. Moreover, under the same liquid phase loading, the average liquid film thickness gradually decreased as the helix pitch (W) increased, and the liquid-bridge morphology tended to become elongated. This behavior occurred because a larger pitch stretched the liquid-bridge. To minimize the overall surface energy, the bridge contracted at the center and expanded at both ends, forming an elongated structure. A more elongated liquid-bridge provides a larger gas–liquid interfacial area, which enhances mass and heat transfer between phases and reduces the amount of spiral material required, thereby lowering equipment costs. Additionally, under identical liquid phase loading, the average liquid film thickness progressively increased with larger wire diameter (d). This increase was attributed to the expanded solid–liquid contact area resulting from a larger wire diameter. The enhanced lateral expansion capability of the liquid-bridge led to greater average liquid film thickness and a larger flow cross-sectional area. Therefore, wires with larger wire diameters can withstand higher liquid phase loads. In practical applications, it is advisable to choose wires with the smallest feasible wire diameter while meeting liquid phase load requirements. This strategy reduces gas–liquid mass transfer resistance, increases the renewal rate of the liquid surface, and conserves material.

3.2.3. Gas–liquid contact area

Fig. 9 shows the variation of the gas–liquid contact area in the micro-scale spiral structure with respect to liquid phase loading. The results indicated that the gas–liquid contact area gradually increased as the liquid phase loading rose. As the diameter of the spiral structure increased, the gas–liquid contact area of the liquid-bridge also increased slightly. At the same liquid phase loading, the gas–liquid contact area was observed to increase gradually with larger pitch values (W). This trend can be attributed to the elongation of the liquid-bridge, which provided a larger interfacial area. Similarly, at constant liquid phase loading, the gas–liquid contact area increased with greater wire diameter (d). The increase in wire diameter enhanced the lateral expansion

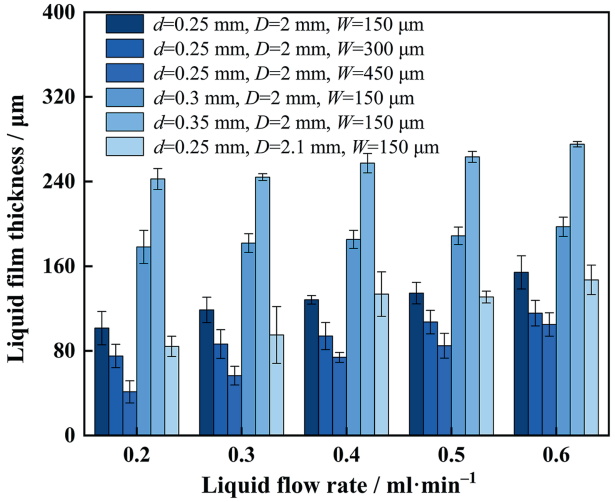


Fig. 8. Trends in average liquid film thickness.

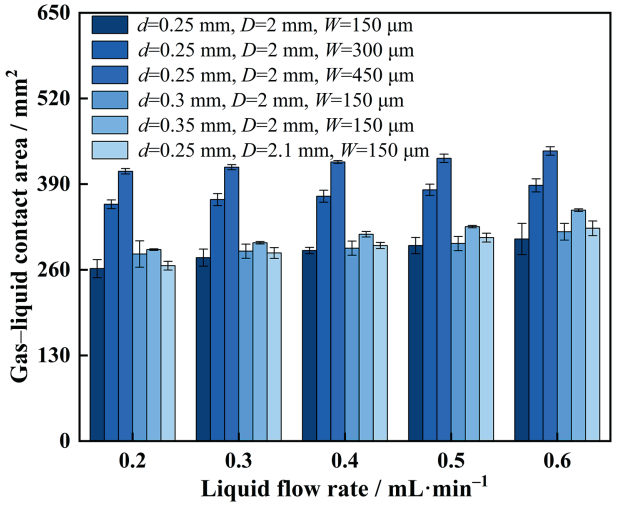


Fig. 9. Gas–liquid contact area as a function of liquid phase load.

capability of the liquid-bridge, resulting in a greater average liquid film thickness. To minimize the overall surface energy, the side profile adapted through an increase in the curvature of the liquid-bridge boundary and an extension of the arc length in the cross-section, thereby progressively enlarging the gas–liquid contact area. Notably, the pitch was found to have the most significant influence on the contact area. In summary, to enhance mass transfer efficiency, it is recommended to prioritize an increase in the helical gap width (W). This approach reduces liquid film thickness, expands the mass transfer area, and lowers mass transfer resistance.

3.2.4. Average residence time

Adequate liquid residence time was essential to ensure sufficient mass and heat transfer. As shown in Fig. 10, the average residence time of the liquid decreased as the liquid phase loading increased. The decrease was particularly rapid at lower loadings and became more gradual at higher values. This behavior occurred because the liquid-bridge was strictly confined within the helical gaps, resulting in a fixed flow path characteristic of piston flow. The residence time was inversely proportional to the flow velocity, and its rate of change was inversely proportional to the square of

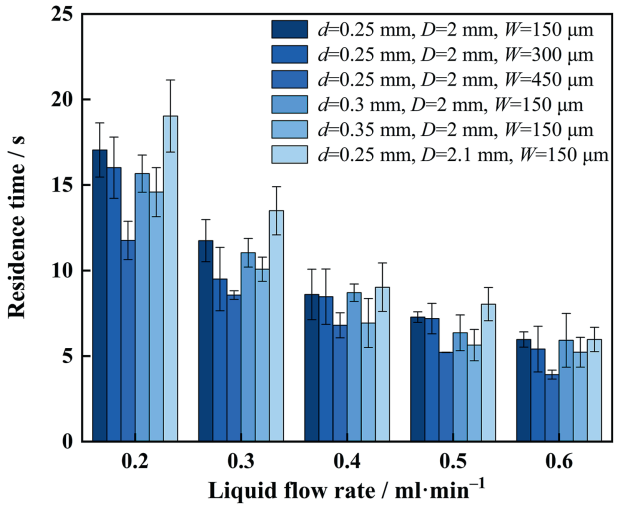


Fig. 10. Average residence time as a function of liquid phase load.

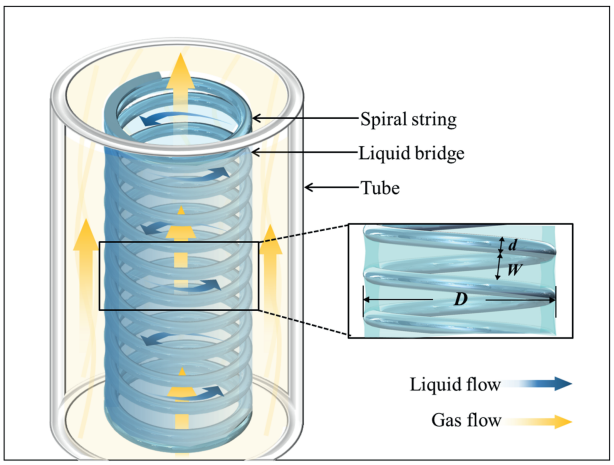


Fig. 11. Schematic diagram of two-phase mass transfer process.

the velocity. Therefore, the residence time declined rapidly at low flow rates and more slowly at high flow rates.

Under identical liquid phase loading conditions, the residence time decreased with increases in either the helical pitch (W) or the wire diameter (d). A larger pitch or wire diameter reduced the helical length per unit channel, shortening the flow path of the liquid-bridge and thus lowering the residence time. In contrast, a larger helical diameter extended the flow path, increasing the residence time. In summary, the pitch, wire diameter, and helical diameter of the micro-scale spiral influenced the average residence time by altering the length of the flow path. Therefore, the use of a smaller pitch, finer wire diameter, and larger helical diameter helped prolong the average residence time of the microscale helical liquid-bridge flow, providing longer gas–liquid contact time and improving mass and heat transfer performance.

3.3. Mass transfer performance

The gas–liquid mass transfer process in microscale helical liquid-bridge flow is illustrated in Fig. 11. In this process, the liquid phase flowed downward along the spiral in the form of a falling liquid film, while the gas phase moved countercurrently through both the internal and external channels of the helix. The flow pattern of the gas phase critically influenced mass transfer performance. In addition, liquid phase loading and helical structural parameters (pitch, wire diameter, and helix diameter) significantly affected mass transfer by modifying flow characteristics including liquid-bridge morphology, interfacial renewal frequency, and residence time. Therefore, precise regulation of these operational and structural parameters was essential to achieve efficient mass transfer.

3.3.1. Effect of gas flow patterns

Micro-scale helical liquid-bridge flow features hollow structures with distinct gas–liquid interfaces, enabling gas phase flow through multiple pathways. This study systematically investigates the influence of gas flow paths (internal spiral channels, external channels, and combined internal–external channels) and gas flow rates on mass transfer coefficients. Experiments were conducted with liquid flow rates (Q_L) fixed at 0.2, 0.4, and 0.6 ml·min^{-1}, while total gas flow rates (Q_G) varied at 0.4, 0.5, 0.6, 0.7, and 0.8 ml·min^{-1}. The liquid-phase volumetric mass transfer coefficient for the CO_2–water absorption system, calculated using Eq. (11), is shown in Fig. 12. Under identical liquid flow conditions, the mass transfer coefficient exhibited a slight increase with rising total gas flow rate. This phenomenon stems from the enhanced average mass transfer driving force across the entire tower due to increased gas flow, which promotes CO_2 transfer into the liquid phase, thereby marginally boosting the mass transfer coefficient. Concurrently, in countercurrent operation mode, the elevated total gas flow rate shortens gas residence time and accelerates the renewal of the gas–liquid interface, contributing to a modest enhancement in mass transfer.

Comparing the effects of three gas-phase flow configurations on mass transfer reveals that countercurrent mass transfer using the dual-channel mode (gas flowing simultaneously through both the inner and outer spiral channels) achieves the highest mass transfer coefficient. Using the outer channel yields the second-highest value, while the inner channel produces the lowest. This difference primarily stems from the significant variation in effective gas–liquid contact area. When the gas phase employs dual-channel flow, both the inner surface (inside the liquid-bridge) and outer surface (outside the liquid-bridge) of the liquid-bridge structure are exposed to the flowing gas phase. Compared to modes utilizing only one surface (inner or outer), this nearly doubles the effective gas–liquid contact area. According to fundamental mass transfer principles, this increased gas–liquid contact area directly leads to a significant enhancement in specific surface area and mass transfer coefficient. Furthermore, during dual-channel absorption, the average liquid film thickness is half that of the liquid-bridge, whereas single-channel absorption employs the full thickness. This thinner film further reduces mass transfer resistance, resulting in superior absorption performance for dual-channel systems.

Thus, during CO_2 absorption, increased gas flow rate primarily enhances mass transfer by amplifying the average mass transfer driving force. The gas phase pathway plays a key role by regulating the effective contact area and liquid film thickness. Leveraging the unique semi-constrained flow advantages of liquid-bridge flow, particularly by adopting a dual-channel countercurrent configuration to maximize gas–liquid contact area and minimize average liquid film thickness, constitutes a key strategy for achieving high-efficiency mass transfer performance.

3.3.2. Effect of liquid flow rate

This study investigated the effect of liquid flow rate on the mass transfer coefficient under gas flow rates ranging from 0.2 to 0.6 ml·min^{-1} and under countercurrent gas–liquid (dual-channel)

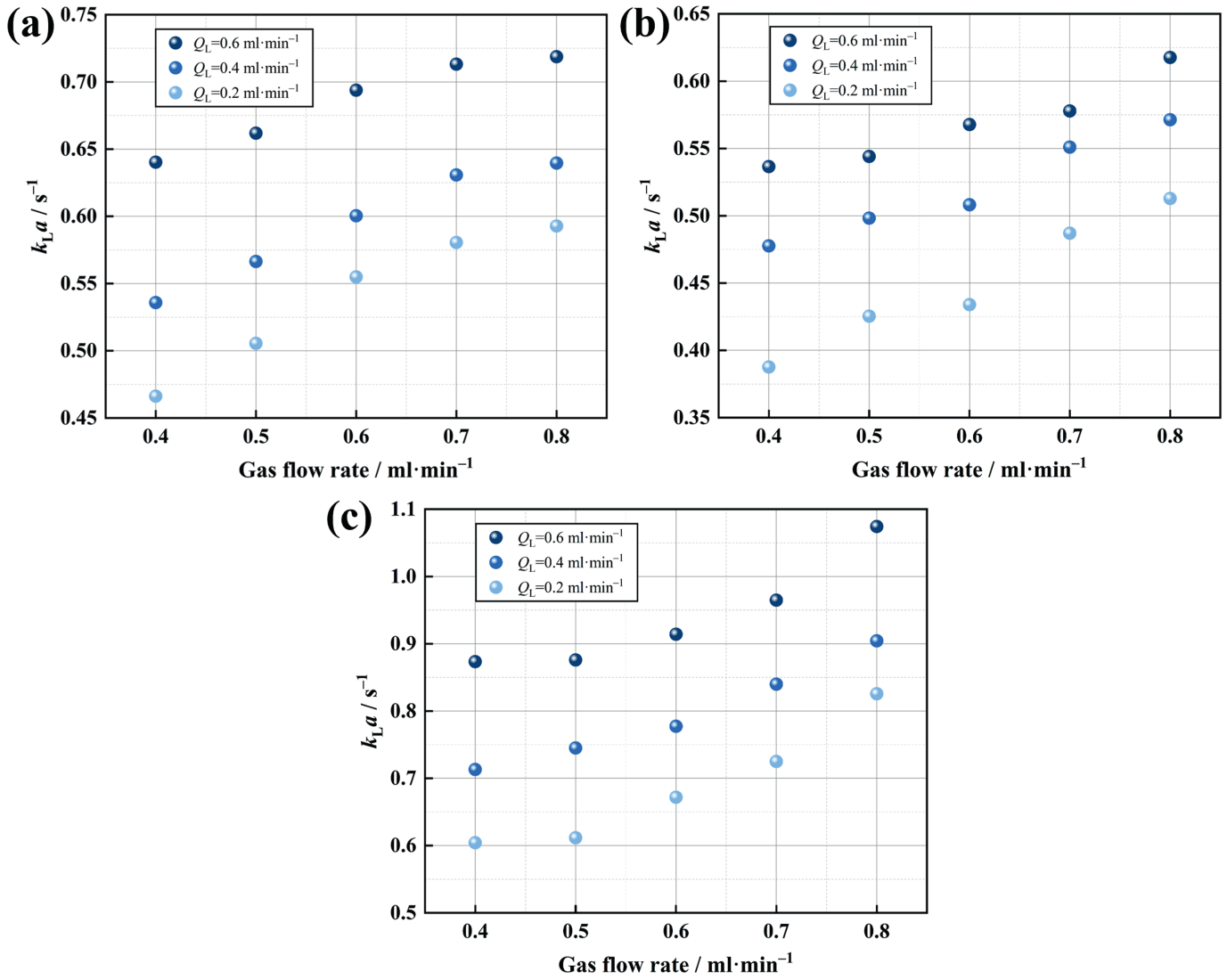


Fig. 12. Effects of gas flow configuration on mass transfer processes: (a) outer channel, (b) inner channel, (c) dual-side channel.

conditions. The results indicated that the mass transfer coefficient significantly increased with rising liquid flow rate at any given gas flow rate (Fig. 13). An increased liquid flow rate enhanced the bulk flow velocity within the liquid-bridge, intensified fluid shear stress, and accelerated the renewal frequency of the liquid film at the gas–liquid interface. This rapid surface renewal effect effectively reduced the thickness of the liquid-phase concentration boundary layer near the interface, thereby increasing the mass transfer coefficient. Simultaneously, the rapid renewal continuously removed high-concentration liquid saturated with CO_2 from the interface while replenishing it with fresh low-concentration liquid. This process maintained a low CO_2 concentration within the interfacial liquid film, strengthening the mass transfer driving force. Furthermore, increased liquid flow caused lateral expansion of the liquid-bridge boundary, which was manifested as an increase in the left and right chord lengths of the bridge. This expansion directly increased the effective gas–liquid contact area, further enhancing the overall mass transfer coefficient.

Thus, within the micro-scale helical liquid-bridge system, an increased liquid flow rate achieved three synergistic effects: accelerated liquid film renewal to reduce the concentration

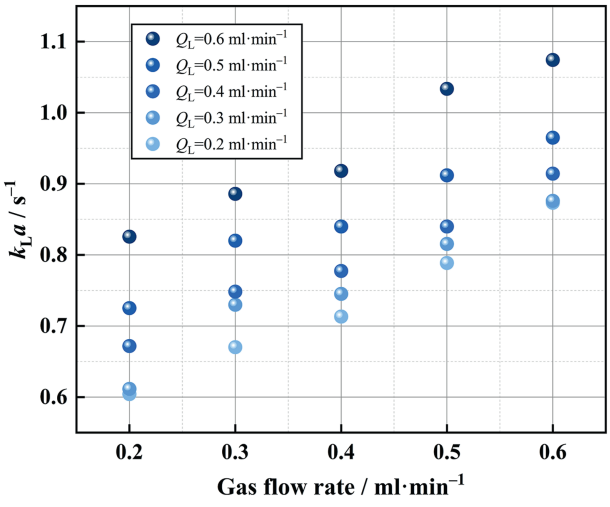


Fig. 13. Effects of liquid flow rate on mass transfer.

boundary layer thickness, sustained low interfacial CO_2 concentration to enhance the mass transfer driving force, and expanded liquid-bridge morphology to increase the effective gas–liquid contact area. These processes were not independent but constituted an interconnected dynamic system. Increased flow velocity drove interface renewal and liquid-bridge deformation, while the expanded surface area provided a broader region for efficient interface renewal. Their combined effects ultimately significantly enhanced the mass transfer efficiency.

3.3.3. Effect of helical parameters

The effect of pitch. The variation of the liquid-phase volumetric mass transfer coefficient with helical pitch is shown in Fig. 14. Experimental results indicated that under identical liquid phase loading, the volumetric mass transfer coefficient increased with greater helix pitch. This is attributed to the fact that increased helix spacing reduces the average liquid film thickness. As the water absorption of carbon dioxide is a liquid film-controlled process, mass transfer resistance is primarily concentrated within the liquid film layer. A thinner liquid film significantly reduces mass transfer boundary layer resistance, thereby promoting the transfer of components from the phase interface into the bulk liquid phase. Additionally, increased helical spacing significantly influences liquid-bridge morphology. Greater pitch elongates liquid-bridges, enhancing the effective gas–liquid contact area per unit volume. The combined effects of thinner liquid films and increased effective gas–liquid contact area drive the rise in the volumetric mass transfer coefficient (k_La). This result aligns with the dual-film theory, which suggests that any operation reducing liquid film thickness or increasing specific surface area enhances mass transfer. The results demonstrate that adjusting the simple structural parameter of helical pitch can effectively enhance mass transfer, providing practical guidance for process intensification and equipment optimization. In practical applications, appropriately increasing the pitch can improve mass transfer efficiency, reduce energy consumption, and enable equipment miniaturization while maintaining processing capacity. This approach is particularly suitable for continuous micro-reaction systems that require high mass transfer rates. It should be noted that increasing the pitch must be done while maintaining the stability and continuity of the liquid-bridge.

The effect of wire diameter. The liquid phase volumetric mass transfer coefficient varied with the spiral wire diameter, as shown in Fig. 15. The results indicated that the liquid phase volumetric mass transfer coefficient exhibited a decreasing trend as the wire diameter increased. This behavior occurred because a larger wire diameter shortened the spiral channel length, thereby reducing the residence time of the fluid within the apparatus. The shorter residence time limited the opportunity for solute to diffuse sufficiently between the phase interface and the bulk liquid phase, which adversely affected the mass transfer process.

Additionally, an increase in wire diameter significantly influenced the liquid-bridge morphology. A larger wire diameter resulted in greater average liquid film thickness and a larger flow cross-sectional area. According to the dual-film theory, the liquid film mass transfer coefficient is inversely proportional to the liquid film thickness. Thus, increased liquid film thickness directly raised the mass transfer resistance in the liquid phase. The expanded flow area also reduced the liquid velocity and interface renewal frequency, further inhibiting mass transfer.

Consequently, under the combined effects of reduced residence time, increased liquid film thickness, and diminished interface renewal capacity, the liquid phase volumetric mass transfer coefficient (k_La) gradually decreased with increasing wire diameter. These results suggest that wire diameter selection requires a balance between mass transfer efficiency and fluid throughput. Although smaller wire diameters facilitate superior mass transfer performance, the processing capacity and operational stability of the unit must also be considered. Therefore, wire diameter parameters should be determined based on the primary objectives of the process.

The effect of diameter. As shown in Fig. 16, the volumetric mass transfer coefficient increased with the spiral diameter. A larger spiral diameter extended the flow path of the liquid-bridge within the device, resulting in a corresponding increase in liquid residence time. This longer residence time provided more time for mass transfer between the gas and liquid phases, facilitating the diffusion of solutes from the interface to the bulk phase, thereby directly enhancing mass transfer efficiency. Secondly, at a constant liquid volume, the increased diameter distributed the same amount of liquid over a longer helical liquid-bridge, reducing the average liquid film thickness. This thinner film significantly lowered mass transfer resistance. Furthermore, the larger diameter altered the morphology of the liquid-bridge, causing it to contract inward and increasing the arc length of its free surfaces. This structural change increased the gas–liquid interfacial area per unit

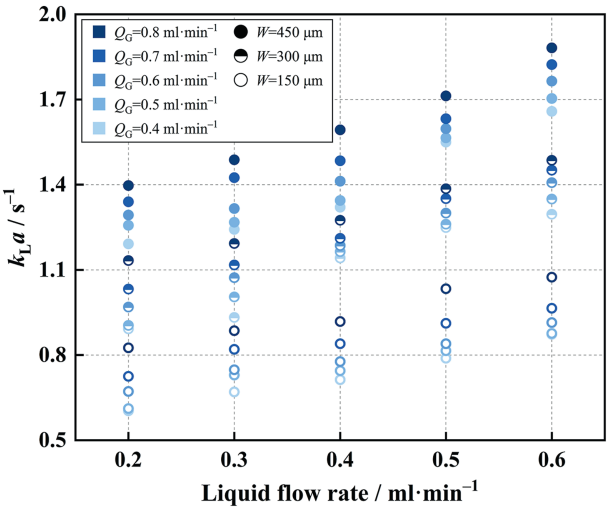


Fig. 14. Effects of helical pitch on mass transfer.

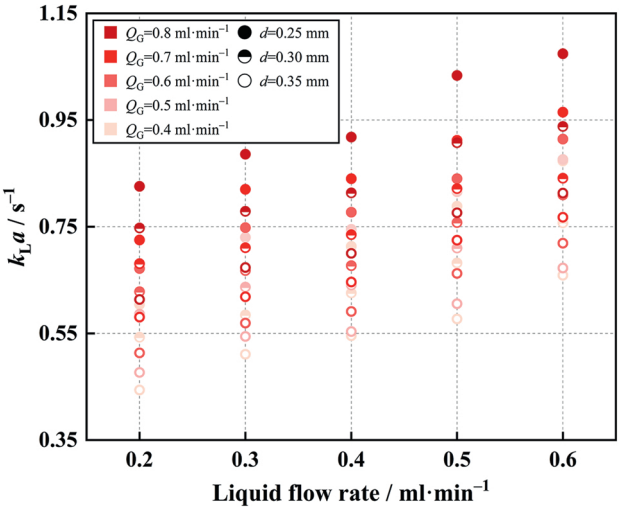


Fig. 15. Effects of wire diameter on mass transfer.

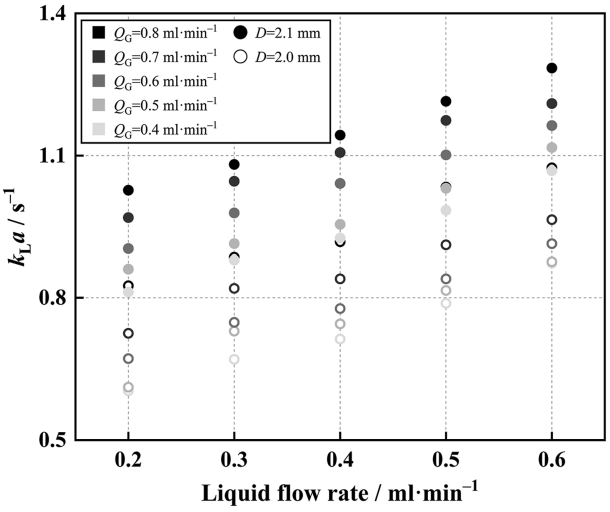


Fig. 16. Effects of helix diameter on mass transfer.

volume. The combined effects of extended residence time, reduced film thickness, and increased specific surface area collectively improved the volumetric mass transfer coefficient with increasing diameter. These findings demonstrate that appropriately increasing the spiral diameter within permissible operating conditions is an effective strategy for enhancing mass transfer.

3.4. Mass transfer coefficient prediction

Numerous studies have focused on developing accurate and broadly applicable theoretical models for predicting the liquid mass transfer coefficient (k_La) in microchannels. Among these, empirical correlations based on dimensionless numbers have been widely adopted due to their capacity to integrate multiple physical parameters and exhibit strong extrapolation capability. Such correlations are typically established by developing separate parameter sets for different flow regimes and performing least-squares regression on experimental data, thereby revealing the physical mass transfer behavior within microchannels under specific flow conditions.

Yue *et al.* [31] proposed an empirical correlation for rectangular microchannels with a hydraulic diameter of 667 μm, formulated in terms of the Sherwood number ($Sh_L = k_L \cdot d_h/D_L$) and the Schmidt number ($Sc_L = \mu_L/(\rho_L D_L)$). Their model incorporated both gas-phase and liquid-phase Reynolds numbers ($Re_G = d_h \cdot u_G \cdot \rho_G/\mu_G$, $Re_L = d_h \cdot u_L \cdot \rho_l/\mu_L$) to account for the relative effects of inertial and viscous forces, as presented in Eq. (13).

$$\frac{Sh_L a d_h}{Sc_L^{0.5}} = 0.0439 Re_G^{0.394} Re_L^{0.905} \tag{13}$$

However, when this model was directly applied to the micro-scale helical structures examined in this study, the predicted values deviated significantly from the experimental values, with discrepancies exceeding 20%. The primary cause of this deviation was attributed to the substantially smaller channel gap used in this study compared to the dimensions employed by Yue *et al.* At this reduced scale, capillary forces became a dominant factor that could not be overlooked [32]. Their influence could be quantified through the capillary number ($Ca = \mu \cdot u/\sigma$). Accordingly, the liquid-phase capillary number Ca_L was introduced, and a new correlation was proposed:

$$\frac{Sh_L a d_h}{Sc_L^{0.5}} = 9.06 \times 10^{-8} Re_G^{0.318} Re_L^{2.75} Ca_L{}^{2.306} \tag{14}$$

By incorporating Ca_L, Sh_L, Sc_L, and Re into the construction of the correlation equation and performing parameter fitting with the least squares method, a new empirical correlation equation suitable for this system was ultimately proposed (Eq. (14)). The applicability range of this empirical equation was Re_L from 5 to 30, Ca_L from 0.003 to 0.016, with water as the liquid phase. As shown in the comparison between experimental and predicted values in Fig. 17, the new correlation demonstrated excellent predictive accuracy, with relative deviations controlled within ±15%. Therefore, this model not only provides a reliable tool for predicting liquid-phase mass transfer coefficients in the current system but also offers a valuable reference for modeling and designing similar microstructure-enhanced mass transfer processes.

3.5. Mass transfer performance comparison

Based on the same gas–liquid absorption system (CO_2–water), this paper compares the mass transfer performance of a novel micro-scale countercurrent gas–liquid absorber with multiple reactor types, with relevant results listed in Table 3. The volumetric mass transfer coefficient (k_La) serves as the core comparison parameter, aiming to eliminate the influence of device size on mass transfer performance. The compared devices include bubble columns, packed columns, absorbers utilizing macro-scale spiral packing, microreactors, and the device described herein. The comparison revealed that the countercurrent absorption device, constructed based on micro-scale helical liquid-bridges, achieved a liquid-phase volumetric mass transfer coefficient one to two orders of magnitude higher than that of conventional large-scale equipment. This substantial improvement was primarily attributed to the exceptionally high specific surface area within the microchannels and the fluid dynamics characteristics under confined conditions. At the sub-millimeter scale, the phase interface density increased dramatically, significantly enhancing the mass transfer driving force. Concurrently, the micro-confined effect effectively suppressed axial backmixing, promoting stable and efficient countercurrent contact between the gas and liquid phases, thereby markedly accelerating mass transfer rates. Notably, the device achieved mass transfer performance comparable to that

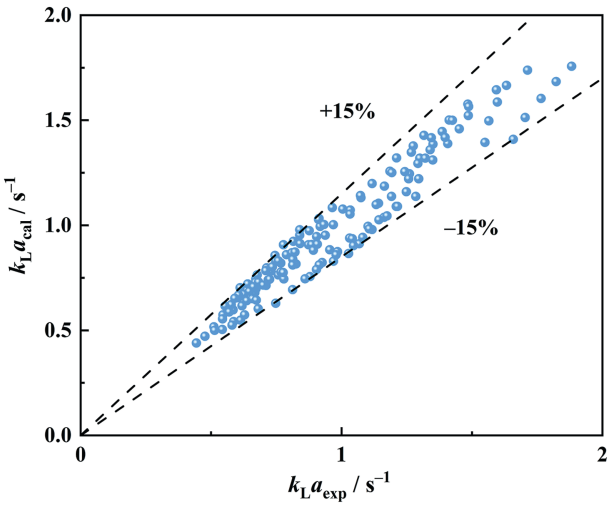


Fig. 17. Comparisons of predicted and actual mass transfer coefficients.

Table 3
Comparison of gas–liquid mass transfer performance.

Reactor type	a/m^{-1}	$k_La \times 10^2/s^{-1}$	Refs.
Bubble column reactor	0.89–600	0.0424–24	[33,34]
Packed columns, concurrent	10–1700	0.04–102	[33,34]
Packed columns, countercurrent	10–350	0.04–7	[33–35]
Conventional-scale helical packing	125–250	0. 6–3	[36]
Microchannel reactor	3400–9000	30–100	[37]
This study	1530–3100	50–200	/

of similar microreactors, demonstrating exceptional interfacial transfer capability. The micro-scale helical liquid-bridge flow not only formed an effective confined flow structure but also enabled continuous, stable countercurrent flow of the gas and liquid phases within the microchannel, enhancing interfacial renewal and mass transfer efficiency. This flow pattern effectively combined the advantages of micro-scale effects and countercurrent operation, demonstrating application potential in high-efficiency gas absorption, continuous microchemical reactions, and integrated process intensification. Consequently, the device structure proposed in this study not only exhibited superior performance but also provided new insights for the future development of high-performance micro-mass transfer systems.

4. Conclusions

This study systematically investigates the flow and mass transfer characteristics of countercurrent gas–liquid absorption technology based on micro-scale helical liquid-bridge flow, revealing its efficient mass transfer mechanism and optimization principles for key operational and structural parameters. Experimental results demonstrate that this device successfully achieves a novel micro-scale countercurrent gas–liquid flow pattern through its unique semi-constrained flow mode. Furthermore, employing dual-channel gas feed fully utilizes both inner and outer surfaces of the liquid-bridge, maximizing effective mass transfer area. Increasing liquid phase velocity enhances surface renewal and expands effective contact area. While ensuring flow stability, appropriately increasing pitch and diameter while decreasing wire diameter helps reduce liquid film thickness, prolong residence time, and increase interfacial area, thereby synergistically intensifying mass transfer. This device achieves a liquid phase volumetric mass transfer coefficient 1–2 orders of magnitude higher than conventional mass transfer equipment. Furthermore, based on experimental data, a dimensionless k_La correlation incorporating the number of liquid phase capillaries was established, with prediction deviations within ±15%. This provides a reliable tool for designing micro-scale mass transfer equipment. This study not only demonstrates the feasibility and superiority of helical liquid-bridge flow in micro-scale countercurrent gas–liquid operations, but also demonstrates low manufacturing costs, excellent economic viability, and long-term stable operation. It provides new insights and theoretical foundations for developing high-performance, low-energy-consumption microchemical separation and reaction processes. Future research should further validate the stability of this device under countercurrent gas–liquid flow across a broader operating range and explore material optimization to enhance its applicability across diverse operational scenarios.

CRediT Authorship Contribution Statement

Liang Yuan: Writing – original draft, Software, Methodology, Data curation, Conceptualization. Xiaoxuan Chen: Writing – original draft, Visualization, Validation, Formal analysis. Haifeng Cong: Writing – review & editing, Resources, Project administration, Methodology, Conceptualization. Xingang Li: Supervision, Resources, Project administration, Funding acquisition.

Declaration of Competing Interest

The authors declare that they have no known competing financial interests or personal relationships that could have appeared to influence the work reported in this paper.

Acknowledgements

The authors acknowledge financial support from the National Nature Science Foundation of China (22378298).

Supplementary Material

Supplementary data to this article can be found online at https://doi.org/10.1016/j.cjche.2026.03.013.

Data Availability Statement

The data that support the findings of this study are available from the corresponding author upon reasonable request.

References

[1] D.Y. Liu, Z. Wang, Y.Y. Cai, J. Chen, J. Jin, B.T. Zhao, Computational fluid dynamics based modeling of gas absorption process: A state-of-the-art review, *Ind. Eng. Chem. Res.* 63 (18) (2024) 7959–8002.
[2] A.D. Vidwans, M.M. Sharma, Gas-side mass transfer coefficient in packed columns, *Chem. Eng. Sci.* 22 (4) (1967) 673–684.
[3] Y.F. Ma, S.S. Zeng, J. Shao, T. Zhou, J.F. Lyu, J.F. Li, P. Lu, An experimental study on gas–liquid two-phase countercurrent flow limitations of vertical pipes, *Exp. Therm. Fluid Sci.* 141 (2023) 110789.
[4] S. Maalej, B. Benadda, M. Otterbein, Interfacial area and volumetric mass transfer coefficient in a bubble reactor at elevated pressures, *Chem. Eng. Sci.* 58 (11) (2003) 2365–2376.
[5] A.M. Dehkordi, C. Savari, Determination of interfacial area and overall volumetric mass-transfer coefficient in a novel type of two impinging streams reactor by chemical method, *Ind. Eng. Chem. Res.* 50 (10) (2011) 6426–6435.
[6] D. Herskowits, V. Herskowits, K. Stephan, A. Tamir, Characterization of a two-phase impinging jet absorber: II. Absorption with chemical reaction of CO_2 in NaOH solutions, *Chem. Eng. Sci.* 45 (5) (1990) 1281–1287.
[7] H.M. Letzel, J.C. Schouten, R. Krishna, C.M. van den Bleek, Gas holdup and mass transfer in bubble column reactors operated at elevated pressure, *Chem. Eng. Sci.* 54 (13–14) (1999) 2237–2246.
[8] Q. Zeng, Y.C. Guo, Z.Q. Niu, W.Y. Lin, Mass transfer coefficients for CO_2 absorption into aqueous ammonia solution using a packed column, *Ind. Eng. Chem. Res.* 50 (17) (2011) 10168–10175.
[9] F. de Meyer, S. Jouenne, Industrial carbon capture by absorption: Recent advances and path forward, *Curr. Opin. Chem. Eng.* 38 (2022) 100868.
[10] Y.H. Yuan, M.H. Han, L.W. Wang, D.Z. Wang, Y. Jin, Mass transfer coefficient for two-phase countercurrent flow in a packed column with a novel internal, *Chem. Eng. J.* 99 (3) (2004) 273–277.
[11] G. Centi, S. Perathoner, The chemical engineering aspects of CO_2 capture, combined with its utilisation, *Curr. Opin. Chem. Eng.* 39 (2023) 100879.
[12] L. Sheng, K. Wang, J. Deng, G.W. Chen, G.S. Luo, Gas–liquid microdispersion and microflow for carbon dioxide absorption and utilization: A review, *Curr. Opin. Chem. Eng.* 40 (2023) 100917.
[13] L. Zhang, J. Yue, Unveiling hydrodynamics in single pellet string microreactors: Insights from gas–liquid slug flow regime and pressure drop, *Chem. Eng. J.* 512 (2025) 162401.
[14] H.Y. Feng, W.Y. He, H. Chen, W.Q. Zhao, C.Y. Zhu, T.T. Fu, Y.G. Ma, Gas–liquid flow and mass transfer characteristics in improved heart-shaped structure microreactor, *Chem. Eng. Process. Process Intensif.* 200 (2024) 109792.
[15] M. Pasha, S.E. Liu, J. Zhang, M. Qiu, Y.H. Su, Recent advancements on hydrodynamics and mass transfer characteristics for CO_2 absorption in microreactors, *Ind. Eng. Chem. Res.* 61 (34) (2022) 12249–12268.
[16] Y.B. Wang, Z.F. Yan, J. Deng, W.H. Duan, G.S. Luo, Gas–liquid microdispersion and countercurrent flow in a miniaturized annular rotating device, *Chem. Eng. J.* 466 (2023) 143210.
[17] D. Gorbunov, M. Nenasheva, G. Shashkin, V. Shapovalov, P. Shvets, E. Naranov, A. Maximov, A. Guda, A. Soldatov, Transferring hydroformylation reaction into high-pressure gas–liquid microfluidic systems: Key achievements and perspectives, *J. Ind. Eng. Chem.* 136 (2024) 46–72.

[18] B. Aghel, E. Heidaryan, S. Sahraie, M. Nazari, Optimization of monoethanolamine for CO_2 absorption in a microchannel reactor, *J. CO_2 Util.* 28 (2018) 264–273.
[19] Y. Chang, Q.C. Shang, L. Sheng, J. Deng, G.S. Luo, Gas–liquid countercurrent flow characteristics in a microbubble column reactor, *Chem. Eng. Sci.* 300 (2024) 120573.
[20] T. Xu, G.L. Wang, C.Y. Bai, M. Chen, J. Li, Y.B. Wang, Micro-dispersion, flow and mass transfer characteristics of high viscosity gas–liquid flow in a miniaturized annular rotating device, *Sep. Purif. Technol.* 362 (2025) 131933.
[21] H.L. Wang, X.D. Li, X.T. Ma, R.C. An, T. Zhang, X.H. Weng, Z.Y. Chang, Dual biomimetic gas–liquid separation system with fluid steering function: Synergistic enhancement to improve separation efficiency, *Sep. Purif. Technol.* 371 (2025) 133167.
[22] B.T. Yin, T.B. Ding, S.L. Wang, Z.Y. Wang, B.J. Sun, W. Zhang, X.L. Zhang, Deformation and migration characteristics of bubbles moving in gas–liquid countercurrent flow in annulus, *Petrol. Explor. Dev.* 52 (2) (2025) 471–484.
[23] H.F. Cong, Z.Y. Zhao, X.G. Li, H. Li, X. Gao, Liquid-bridge flow in the channel of helical string and its application to gas–liquid contacting process, *AIChE J.* 64 (9) (2018) 3360–3368.
[24] L. Yuan, H.F. Cong, X.G. Li, A novel helical descending liquid-bridge for continuous demulsification, *AIChE J.* 69 (11) (2023) e18195.
[25] L. Yuan, Y. Wu, H.F. Cong, X.G. Li, Flow characteristics and multiparameter prediction modeling of cross-scale helical liquid-bridge flows, *AIChE J.* 72 (2) (2026) e70145.
[26] J. Qian, H.J. Gao, Scaling effects of wet adhesion in biological attachment systems, *Acta Biomater.* 2 (1) (2006) 51–58.
[27] M.A. Fortes, Axisymmetric liquid bridges between parallel plates, *J. Colloid Interface Sci.* 88 (2) (1982) 338–352.
[28] D. Lokhat, A.K. Domah, K. Padayachee, A. Baboolal, D. Ramjugernath, Gas–liquid mass transfer in a falling film microreactor: Effect of reactor orientation on liquid-side mass transfer coefficient, *Chem. Eng. Sci.* 155 (2016) 38–44.
[29] H.C. Zhang, G.W. Chen, J. Yue, Q. Yuan, Hydrodynamics and mass transfer of gas–liquid flow in a falling film microreactor, *AIChE J.* 55 (5) (2009) 1110–1120.
[30] J.F. Chen, G.Z. Chen, J.X. Wang, L. Shao, P.F. Li, High-throughput microporous tube-in-tube microreactor as novel gas–liquid contactor: Mass transfer study, *AIChE J.* 57 (1) (2011) 239–249.
[31] J. Yue, G.W. Chen, Q. Yuan, L.A. Luo, L.G. Hervé, Mass transfer in gas–liquid flow in microchannels, *CIESC J* 57 (6) (2006) 1296–1303. (in Chinese)
[32] X.Y. Ji, Y.G. Ma, T.T. Fu, C.Y. Zhu, D.J. Wang, Experimental investigation of the liquid volumetric mass transfer coefficient for upward gas–liquid two-phase flow in rectangular microchannels, *Braz. J. Chem. Eng.* 27 (4) (2010) 573–582.
[33] J.C. Charpentier, Mass-transfer rates in gas–liquid absorbers and reactors, *Adv. Chem. Eng.* 11 (1981) 1–133.
[34] J. Elhajj, M. Al-Hindi, F. Azizi, A review of the absorption and desorption processes of carbon dioxide in water systems, *Ind. Eng. Chem. Res.* 53 (1) (2014) 2–22.
[35] P.V. Danckwerts, Insights into Chemical Engineering, Elsevier, Amsterdam, 1981.
[36] Z. Zhang, H.M. Han, H.F. Cong, X.G. Li, Z.W. Han, Liquid-bridge flow on a vertical spiral spring and its mass transfer characteristics, *Chem. Eng. Sci.* 275 (2023) 118738.
[37] J. Yue, G.W. Chen, Q. Yuan, L.G. Luo, Y. Gonthier, Hydrodynamics and mass transfer characteristics in gas–liquid flow through a rectangular microchannel, *Chem. Eng. Sci.* 62 (7) (2007) 2096–2108.